Nano Energy 121 (2024) 109194

Contents lists available at ScienceDirect

Nano Energy

journal homepage: www.elsevier.com/locate/nanoen

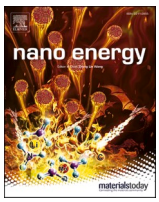

Enhancing performance of triboelectric nanogenerator by accelerating the charge transfer strategy☆

Yushan Sun [a,b,1], Yang Yu [a,c,1], Qi Gao [a,c,1], Xiaosong Zhang [a,c], Jiacheng Zhang [a], Yuqi Wang [a,c], Siyang He [a,c], Hengyu Li [a,c,*], Zhong Lin Wang [a,d,*], Tinghai Cheng [a,c,*]

[a] Beijing Institute of Nanoenergy and Nanosystems, Chinese Academy of Sciences, Beijing 101400, China
[b] School of Mechatronic Engineering, Changchun University of Technology, Changchun 130012, China
[c] School of Nanoscience and Engineering, University of Chinese Academy of Sciences, Beijing 100049, China
[d] Georgia Institute of Technology, Atlanta, GA 30332-0245, United States

ARTICLE INFO

Keywords:
Triboelectric nanogenerator
Charge transfer
High performance
Magnetic field modulation
Bidirectional rotating
Energy harvesting

ABSTRACT

Developing high-performance triboelectric nanogenerators (HP-TENGs) is paramount for expanding their commercial utility. Presently, HP-TENGs predominantly concentrate on augmenting surface charge density. Here, we introduce an innovative strategy, denoted ACT-TENG (Accelerated Charge Transfer TENG), which markedly enhances TENG's performance by effectively accelerating charge transfer between materials, all while preserving the original charge density. We substantiate the feasibility of this approach through systematic investigations, employing magnetic field modulation and bidirectional rotation mode to verify the gain effect of ACT-TENG. Notably, compared to conventional free-standing TENG (FS-TENG), ACT-TENG achieves a 4-fold increase in charge transfer rate and a remarkable 14.6-fold enhancement in output power. This leads to an impressive average power density of 499.05 mW m^{-2} Hz^{-1} , showcasing superior performance compared to previously reported FS-TENG designs. Furthermore, ACT-TENG exhibits exceptional characteristics when deployed in a water flow environment, generating the power of 10.76 mW at a flow rate of 180 L min^{-1}. Finally, we utilize ACT-TENG to harvest energy from water flow, constructing a self-powered Internet of Things (IoT) system within the underground pipeline gallery. This study addresses existing limitations in TENG technology and offers valuable insights into further advancements in enhancing TENG's performance.

1. Introduction

The rapid proliferation of the Internet of Things (IoT) and the explosion of big data have generated an unprecedented demand for distributed sensors [1–3]. However, powering such an expansive sensor network presents a formidable challenge [4]. In light of the constraints posed by limited energy storage and the environmental concerns associated with chemical batteries, harnessing clean energy sources from the environment to drive electronic devices has emerged as an increasingly viable solution [5,6]. In 2012, Wang and colleagues pioneered the technology of triboelectric nanogenerators (TENG) based on the principles of triboelectrification and electrostatic induction [7–12]. This innovative approach allows the conversion of mechanical energy from various environmental sources, including wind [13,14], water [15,16], vibration [17,18], and wave energy [19,20], into electrical output. TENG technology offers several distinct advantages, including cost-effective manufacturing [21,22], a wide range of material options [23,24], and a streamlined production process [25]. These attributes underscore its potential as an enduring and self-sustaining distributed power source.

Since the inception of triboelectric nanogenerators (TENGs), they have been categorized into four distinct operational modes [26–28]. Among these, the free-standing TENG (FS-TENG) has garnered substantial attention from the research community due to its demonstrated

☆ Prof Zhong Lin Wang, an author on this paper, is the Editor-in-Chief of Nano Energy, but he had no involvement in the peer review process used to assess this work submitted to Nano Energy. This paper was assessed, and the corresponding peer review managed by Professor Chenguo Hu, also an Associate Editor in Nano Energy

* Corresponding authors at: Beijing Institute of Nanoenergy and Nanosystems, Chinese Academy of Sciences, Beijing 101400, China.
E-mail addresses: lihengyu@binn.cas.cn (H. Li), zhong.wang@mse.gatech.edu (Z.L. Wang), chengtinghai@binn.cas.cn (T. Cheng).
[1] These authors contributed equally to this work.

https://doi.org/10.1016/j.nanoen.2023.109194
Received 30 October 2023; Received in revised form 28 November 2023; Accepted 13 December 2023
Available online 17 December 2023

superiority in triboelectrification efficiency and amplified output power [29,30]. Nonetheless, in order to extend the practical applicability and expedite the commercial adoption of TENGs, a compelling need exists to further enhance their output performance [31]. A widely accepted premise within the research community posits that the output power of TENGs exhibits a direct proportionality to the square of the surface charge density of the utilized material [32–34]. Consequently, scholarly endeavors have been systematically directed towards optimizing surface charge density, culminating in the proposal of diverse strategies, including material enhancements [35], surface modifications [36], and charge pumping techniques [37,38]. These multifaceted approaches have overwhelmingly contributed to enhancing TENGs' output performance. Nevertheless, it is paramount to recognize that the critical determinant of TENGs' power output resides in the quantity of charge transferred per unit time. Beyond the influence of surface charge density on TENGs, the charge transfer rate holds profound significance [8]. Therefore, accelerating the charge transfer between materials would be a novel and practical approach for constructing high-performance TENGs.

In this work, we present a novel strategy for enhancing the performance of TENGs, denoted ACT-TENG (Accelerated Charge Transfer TENG). ACT-TENG harnesses the charge transfer rate between materials to significantly augment power output in FS-TENG mode. The performance gain of ACT-TENG is meticulously verified through both the magnetic field modulation mechanism and bidirectional rotation mode. The findings indicate that the pulse frequency of the electrical signal experiences a four-fold increase, while the power output and collected energy exhibit remarkable improvements, with a 14.6-fold and 13.9-fold increase, respectively, when compared to conventional FS-TENG. Moreover, ACT-TENG's power density reaches approximately 500.00 mW m^{-2} at 1.0 Hz. To validate the practical utility of this approach, we have designed an integrated device based on ACT-TENG to harvest energy from pipeline water flow. The peak power of this device attains 10.76 mW at a flow rate of 180 L min^{-1}. In addition, we have developed a self-powered monitoring system for an underground pipe gallery based on ACT-TENG, encompassing fire protection, environmental monitoring, and intrusion alarm systems. Importantly, ACT-TENG is not limited to water flow energy harvesting and promises to realize a diverse array of applications in other fields, such as wind energy harvesting, high-voltage power supply, and self-powered sensing. This study introduces an innovative and efficient method for attaining substantial power output from TENGs while concurrently harnessing environmental energy for a distributed energy supply.

2. Results and discussion

2.1. Implementation strategy of ACT-TENG

The four operational modes of the triboelectric nanogenerator (TENG) share a common process for electricity generation. This process

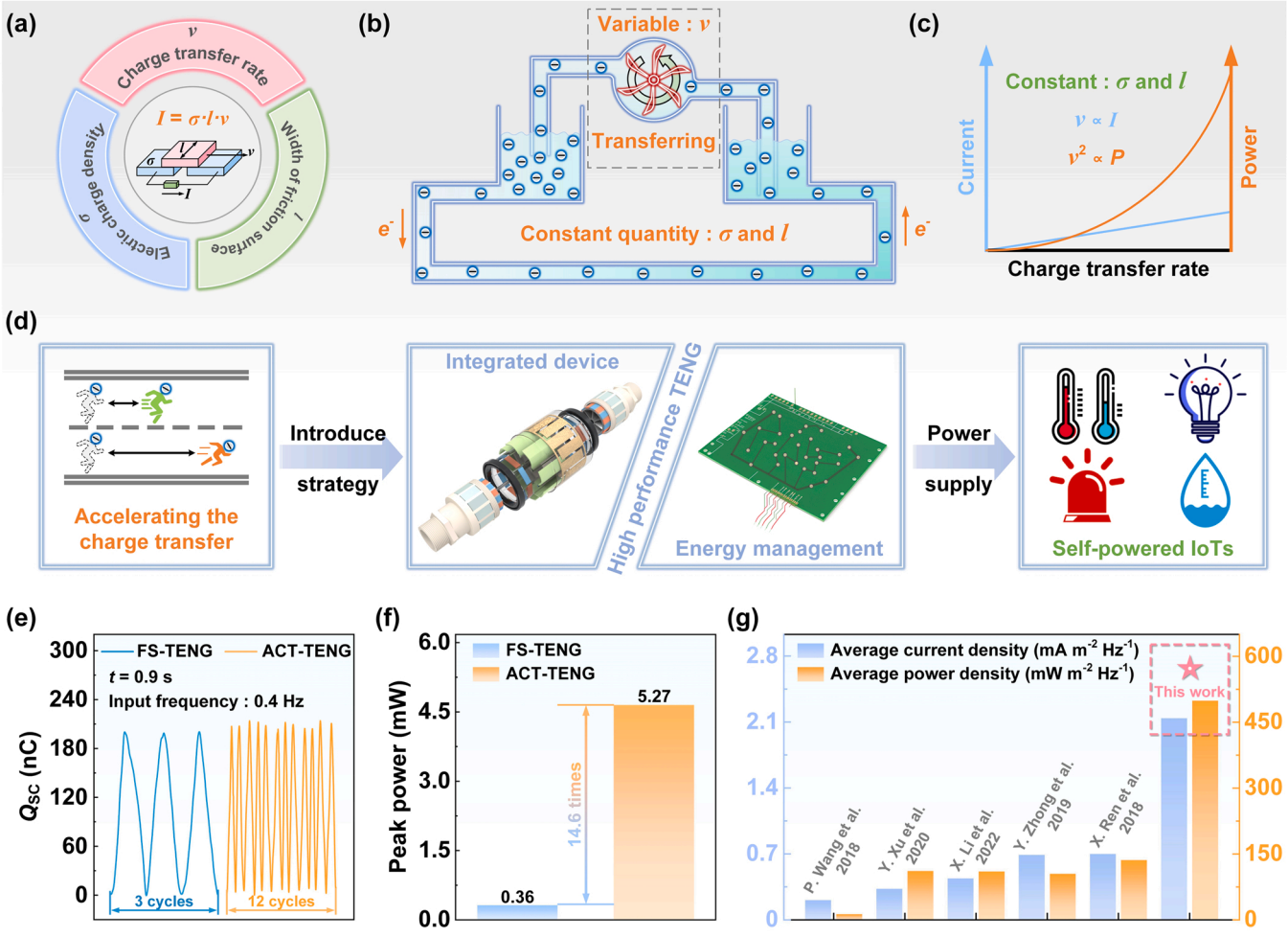

Fig. 1. Mechanism and electrical performance of the ACT-TENG. (a) Fundamental schematic of FS-TENG. (b) Hydraulic turbine analogy for FS-TENG operation. (c) Schematic illustration of charge transfer rate and friction material output performance relationship. (d) Self-powered IoT systems utilizing ACT-TENG devices. (e) Comparative analysis of transferred charge among different TENG modes. (f) Comparative evaluation of peak power output among different TENG modes. (g) Comparative analysis of average current density and power density for ACT-TENG versus other FS-TENG reports.

involves the generation of electrostatic charges through tribo-electrification, the separation of these charges through mechanical motion, and the subsequent creation of induced currents between two objects. In comparison to the other operational modes, the free-standing TENG (FS-TENG) stands out as the mode most likely to produce sustained power output and is easier to understand the power generation process. Its power output is primarily determined by factors such as the charge density of the friction surface (σ), the width of the friction surface (l), and the charge transfer rate (v), as illustrated in Fig. 1a. It is noteworthy that when σ and l are held constant, v emerges as the pivotal factor influencing the TENG's output performance. To provide a clearer perspective on the working mechanism, Fig. 1b presents an analog model akin to a hydraulic turbine. Assuming that all other variables within the system remain constant, the velocity of the water flow channeled by the turbine determines the flow rate through the pipeline, i.e., higher velocity results in an increased flow rate. Consequently, the charge transfer rate v bears a direct proportionality to TENG's output current. The v^2, square of this rate, is directly proportional to TENG's output power, as depicted in Fig. 1c. Essentially, in accordance with Eq. (1), enhancing TENG's performance can be achieved by effectively reducing the charge transfer time.

$$I = \frac{dQ}{dt} \tag{1}$$

In this study, we introduce an innovative strategy termed Accelerated Charge Transfer TENG (ACT-TENG). Integrating this strategy into a device and coupling it with an energy management circuit demonstrates the creation of a high-performance TENG capable of powering essential components in self-powered IoT systems, as exemplified in Fig. 1d. Experimental validation, facilitated by a carefully designed structure, reveals that, under identical mechanical input conditions, the ACT-TENG achieves a noteworthy 4-fold increase in electrical signal pulse frequency (Fig. 1e) and an impressive 14.6-fold surge in peak power (Fig. 1f) when compared to the conventional FS-TENG. Notably, in contrast to a similar FS-TENG previously reported, the ACT-TENG achieves an average current density and average power density of 2.14 mA m^{-2} Hz^{-1} and 449.05 mW m^{-2} Hz^{-1}, respectively, demonstrating exceptional output performance, as depicted in Fig. 1g.

2.2. Working principle of ACT-TENG

To validate the accelerated charge transfer strategy, we develop an ACT-TENG using the magnetic field modulation mechanism and bidirectional rotation mode based on the conventional FS-TENG. The design,

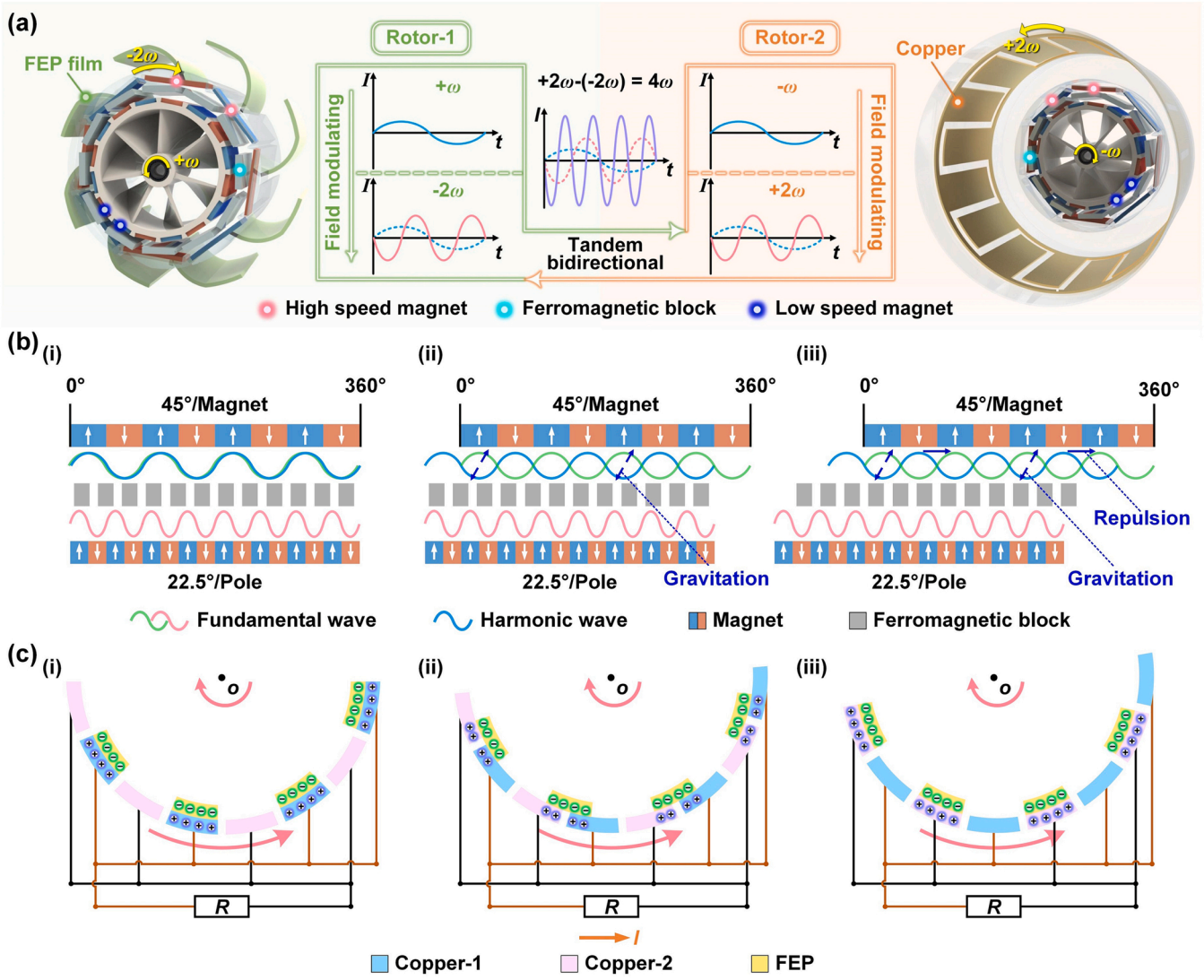

Fig. 2. Working mechanism of the ACT-TENG. (a) Rotor structural design and operational concept. (b) Fundamental principles of magnetic field modulation. (c) ACT-TENG operational mechanism.

illustrated in Fig. 2a, incorporates two sets of magnetic gears with opposing rotations. Each group comprises four pairs of high-speed magnets with opposite polarity, twelve ferromagnetic blocks, and eight pairs of low-speed magnets with opposing polarity. The operational concept is as follows: Firstly, assuming the rotor of the conventional FS-TENG rotates at an angular velocity of $+\omega$ or $-\omega$, we introduce magnets and ferromagnetic blocks to achieve magnetic field modulation, enabling a transmission ratio between the magnetic gears of 1:2. Consequently, the angular velocity of the high-speed magnets increases to -2ω or $+2\omega$. Finally, the arrangement of two sets of rotating magnetic gears with opposite rotations along the same axis results in relative angular speeds of 4ω. By affixing different friction materials to each of the two sets of rotors, the charge transfer rate theoretically increases fourfold, consequently boosting the output current and pulse frequency by the same factor.

Fig. 2b provides a simplified two-dimensional representation of magnetic field modulation. To aid in analysis, we have transformed the intricate three-dimensional model into a radial cross-section. Initially, as shown in Fig. 2b(i), a fundamental wave (pink) with eight wavelengths appears between the low-speed magnet and the ferromagnetic block. The ferromagnetic block fine-tunes the magnetic field, resulting in a four-harmonic wave (blue) with different wavelengths in the opposing space. Simultaneously, the high-speed magnet produces a four-wavelength fundamental wave (green). When the magnetic fields of the low-speed and high-speed magnets are 180 degrees out of phase, as illustrated in Fig. 2b(ii), they remain stable due to the mutual attraction between opposite polarities. As the low-speed rotor moves the low-speed magnet to the left, the pink fundamental wave shifts leftward, while the magnetic field produced by the ferromagnetic block (blue harmonic) moves in the opposite direction (rightward). This interaction causes repulsive forces to act on the leading peak of the green fundamental wave and attractive forces on the entire trough of the blue harmonic. Consequently, the inherent magnetic field of the high-speed magnet shifts to the right, and the high-speed rotor moves accordingly, as depicted in Fig. 2b(iii). It is important to note that the blue harmonic has a wavelength twice that of the pink fundamental, allowing the high-speed rotor to complete two full circles in the opposite direction for each revolution of the low-speed rotor, resulting in a frequency increase effect.

The working principle of the ACT-TENG is shown in Fig. 2c. Initially, the FEP film overlaps with copper-1, t leading to a positive charge on copper-1 and an induced negative charge on the FEP film (Fig. 2c(i)). As illustrated in Fig. 2c(ii), electrostatic equilibrium is disrupted when the FEP film and the copper electrode move in opposite directions. The FEP film contacts copper-2, causing electrons to flow from copper-2 to copper-1 through the external circuit. This process gradually accumulates positive charges on the surface of copper-2. As the rotors continue moving, the FEP film completely overlaps with the copper-2, and the electrons neutralize all the positive charges on the copper-1 to achieve electrostatic balance, as shown in Fig. 2c(iii). As the rotors further move, the FEP film slides from copper-2 to copper-1, and the electrons in copper-1 flow into copper-2, reversing the current direction in the circuit. This cycle repeats, allowing the TENG to generate continuous alternating current. The bidirectional rotation of the rotors accelerates the production of alternating current. To elucidate the operational mechanism of the TENG, we employed COMSOL finite element simulation to illustrate the continuous variation of the open-circuit voltage (V_{OC}), depicted in Fig. S1. V_{OC} is precisely defined as the potential difference between adjacent electrodes. When two friction materials move in opposite directions, the potential difference undergoes a cycle from maximum to minimum and back to maximum. The results affirm the congruence between the observed potential distribution and the theoretical mechanism analysis.

2.3. Electrical properties of ACT-TENG

To evaluate the effectiveness of the proposed strategy, we devised three modes for comparative experiments, as illustrated in Fig. 3a. Mode-A represents the FS-TENG, while mode-B incorporates the magnetic gear up-frequency mechanism, and mode-C showcases the ACT-TENG. Firstly, the designed magnetic gears are structurally optimized. Fig. 3b illustrates the length of the low-speed magnet (L_1) and the high-speed magnet (L_2). In this experiment, L_2 is set to 10 mm, and the impact of the length ratio between L_1 and L_2 on the magnetic field modulation results is investigated. We conduct experiments to examine the speed ratio between the high-speed and low-speed rotors under varying input frequencies of the rotating motor. The transmission ratio between the inner and outer rotors is set to 1:2, meaning the speed ratio should ideally remain stable at two under different input frequencies. The experimental results show that the desired characteristics are achieved when the length ratio between L_1 and L_2 is set to 2 and 3, as shown in Fig. 3c. However, for length ratios of 1 and 0.5, the speed ratio dropped to 0 within specific input frequency ranges. This is due to the high-speed rotor's inability to overcome the torque between the magnetic fields, resulting in a complete halt of rotation. To further refine the choice between 2 and 3 length ratios, the average torque produced by the two length ratios at different input frequencies was evaluated, as illustrated in Fig. 3d. The experimental results indicate that a length ratio of 2 produces significantly lower average torque than a length ratio of 3. Consequently, a length ratio of 2 emerges as the optimal choice for a comprehensive comparison.

After determining all the experimental parameters, three modes are compared. The input frequency of the rotating motor is controlled, and the V_{OC} obtained by the three modes is analyzed using a fast Fourier transform (FFT) to determine the pulse frequency. As the input frequency increases from 0.2 Hz to 1.0 Hz, the pulse frequency of mode-A increases from 1.60 Hz to 7.97 Hz, mode-B from 3.18 Hz to 15.97 Hz, and mode-C from 6.49 Hz to 31.94 Hz, as shown in Fig. 3e. The order of pulse frequency from smallest to largest was mode-A, mode-B, and mode-C. Subsequently, the short-circuit current (I_{SC}) of the three modes is tested under different input frequencies. The results follow a consistent trend with the pulse frequency. As the input frequency increases from 0.2 Hz to 1.0 Hz, the I_{SC} of mode-A increases from 1.25 μA to 6.00 μA, mode-B from 2.50 μA to 12.75 μA, and mode-C from 4.70 μA to 22.60 μA (Fig. 3f). Fig. 3g demonstrates that mode-B's pulse frequency and I_{SC}, obtained by magnetic field modulation of mode-A, increased by approximately two times. Similarly, mode-C's pulse frequency and I_{SC}, obtained through tandem bidirectional arrangement, increased approximately four times. The raw signals of V_{OC}, $I_{SC,}$ and transferred charge (Q_{SC}) for the three modes at different input frequencies can be seen in Fig. S2. Power is also an important metric for evaluating the advantages and disadvantages of a power-generating device. The peak power of the three modes is tested to be 0.36 mW, 1.32 mW, and 5.27 mW at an input frequency of 1.0 Hz, 14.6 times higher peak power in mode-C compared to mode-A, as shown in Fig. 3h. Fig. S3 displays the charging curves of the three modes for capacitors of varying capacitance at an input frequency of 1.0 Hz, while Fig. 3i and S4 show the work done during their charging process. For a 100 μF capacitor, the energy produced by the three modes after 41 s of charging is 0.09 mJ for mode-A, 0.41 mJ for mode-B, and 1.25 mJ for mode-C, indicating a 13.9-fold improvement by mode-C. The above experimental results show that ACT-TENG has a significant advantage in terms of output performance.

Furthermore, it is essential to avoid compromising electromechanical conversion efficiency when striving for performance enhancement. Consequently, the electromechanical conversion efficiencies of the three modes are assessed using Eq. (2). Experimental findings, as depicted in Fig. 3j, indicate enhancements in these efficiencies.

$$\eta = \frac{\overline{I_R^2 R}}{\overline{T\omega}} \tag{2}$$

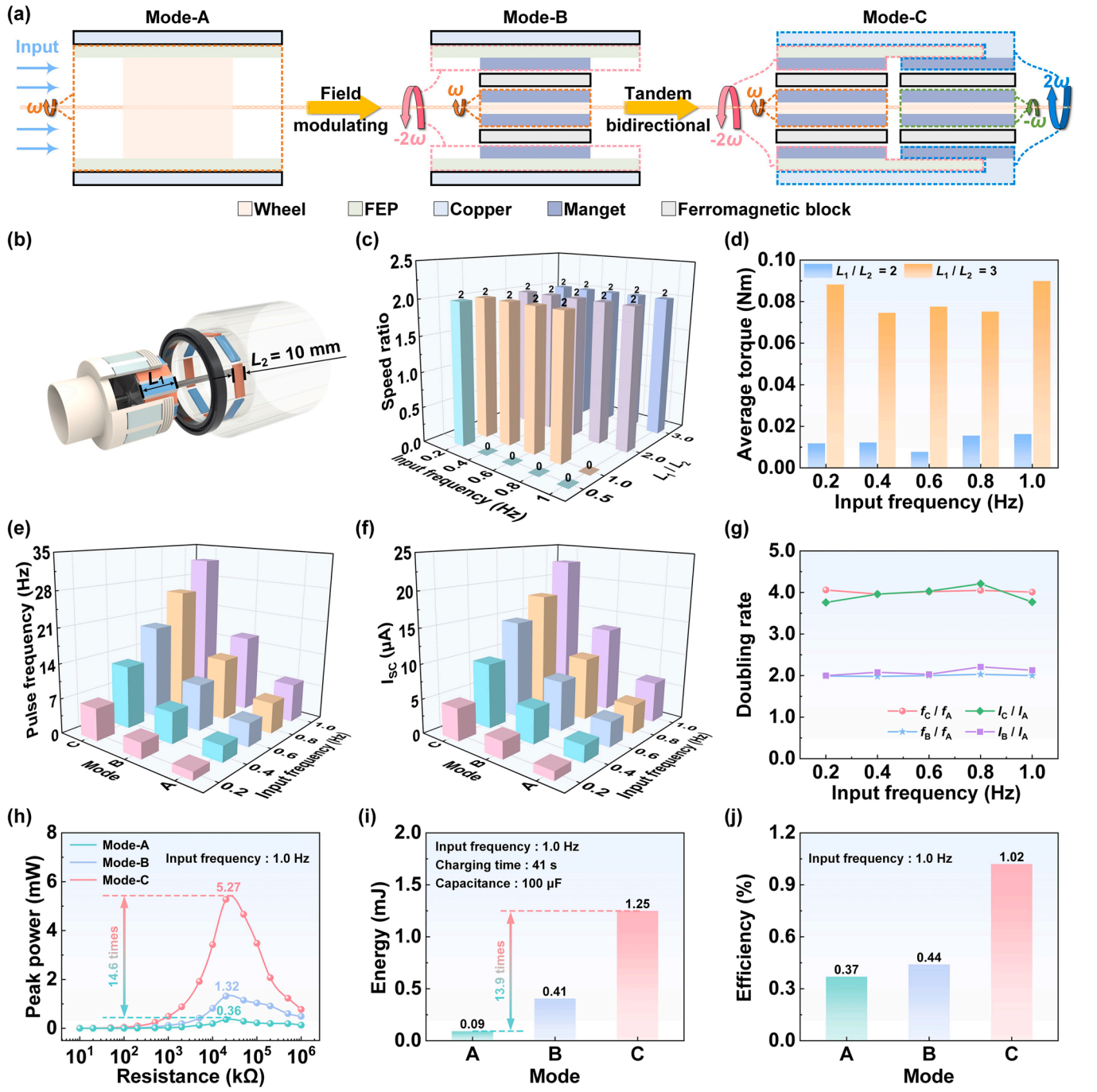

Fig. 3. Comparative analysis of three operation modes under identical conditions. (a) Illustration depicting the three operation modes. (b) Schematic detailing the optimization of magnet length ratios. (c) Speed ratio between high-speed and low-speed rotors at various input frequencies for magnets with different length ratios. (d) Average torque of high-speed rotors at various input frequencies for magnets with varying length ratios. (e) Pulse frequency of the three modes at different input frequencies. (f) I_{SC} of the three modes at varying input frequencies. (g) Doubling rate comparison of I_{SC} and pulse frequency between different modes. (h) Comparison of peak power among different modes at a 1.0 Hz input frequency. (i) Energy generation by the different modes after 41 s of charging at a 1.0 Hz input frequency. (j) Evaluation of electromechanical conversion efficiency of different modes.

where η represents the electromechanical conversion efficiency, I_R stands for the current at the specified load resistance (R), while T denotes the torque applied to drive the prototype, and ω signifies the prototype's angular speed. It is worth noting that efficiency improvements do not exhibit a linear relationship due to variations in operating torques stemming from different structures. However, the effectiveness of our strategy is clearly evident, demonstrating that with a well-considered design, it is possible to achieve common improvements in both performance and efficiency.

3. Applications of the ACT-TENG

3.1. Performance of the ACT-TENG under pipeline conditions

The ACT-TENG boasts a versatile array of applications, encompassing wind and water flow energy harvesting, high-voltage power supply, self-powered sensing, and beyond. In this section, a water flow energy harvesting TENG (WFEH-TENG) is designed based on ACT-TENG to prove its potential in practical applications, and its structure is shown in

an exploded diagram in Fig. 4a. It is worth noting that two water wheels with opposite rotations are designed to collect the kinetic energy of the fluid. Fig. 4b(i) presents a force analysis of the two water wheels and explains the reason for the opposite rotation directions. The subsequent Equation serves as a means to compute the force:

$$F_N = F_F \sin(\theta) \tag{3}$$

$$F_{Ny} = F_N \cos(\theta) = F_F \sin(\theta)\cos(\theta) \tag{4}$$

The fluid driving force (F_F) and its component force towards the chord line's normal direction (F_N) play crucial roles in the system's operation. Additionally, θ represents the installation angle of the blade. F_{Ny} refers to the component force of F_N in the direction of water wheel motion. Referring to Fig. 4b(i), it is observed that the F_{Ny} directions of the two water wheels differ. Specifically, considering the direction of the liquid inlet, F_{Ny1} generates a counterclockwise torque (T_1) along the positive y-axis direction, while F_{Ny2} generates a clockwise torque (T_2) along the negative y-axis direction. Consequently, the two water wheels rotate in opposite directions. The physical photos of the WFEH-TENG and parts are shown in Fig. S5.

First, structural optimization of the water wheel is performed. We define the coverage as the ratio of the projected area of all blades to the effective working area of the water wheel for energy collection when viewed from a projection angle. The impact of different coverage levels

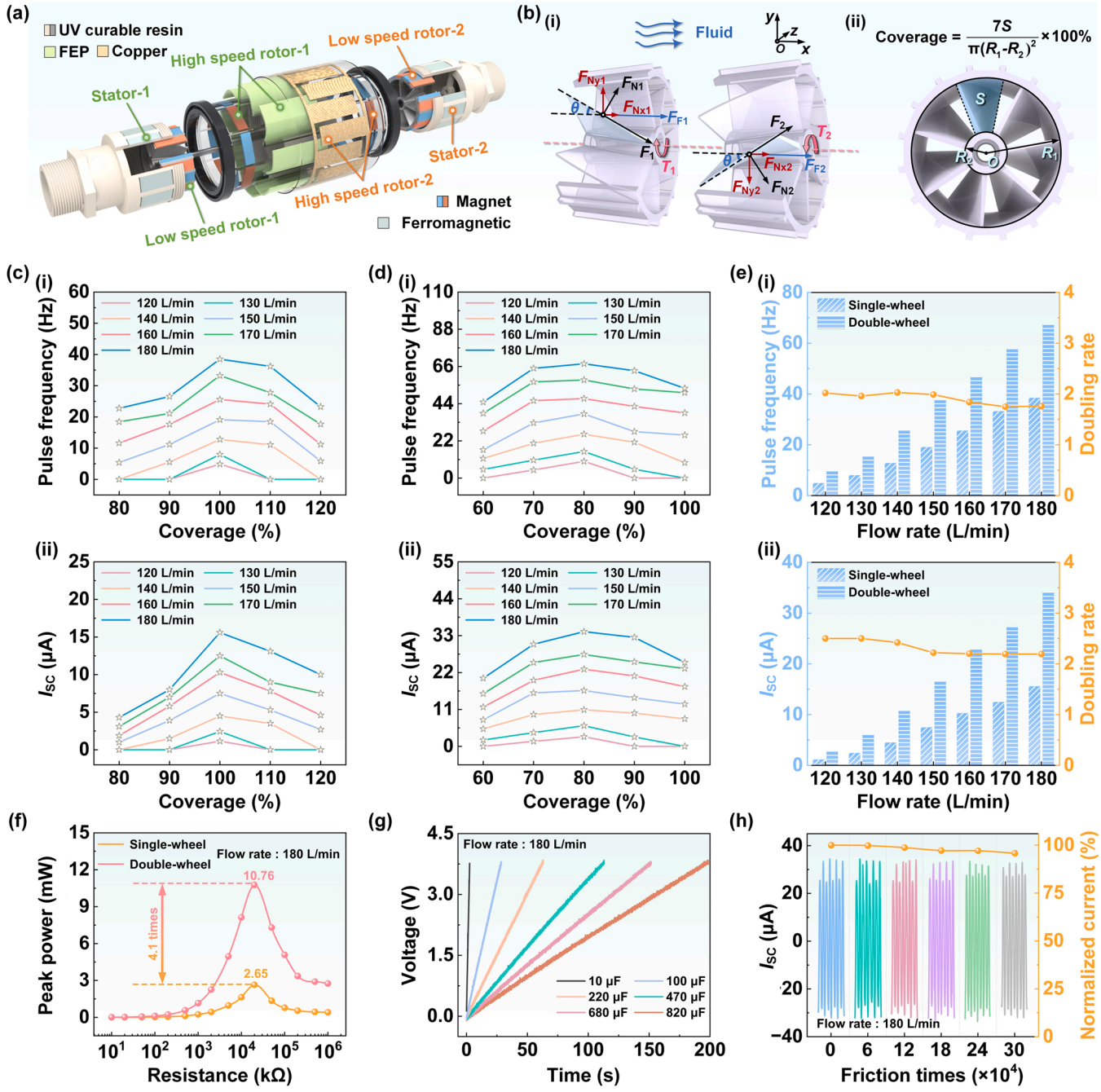

Fig. 4. Applications of the ACT-TENG. (a) Three-dimensional representation of the designed prototype. (b) (i) Detailed rotor structure of the prototype. (ii) Schematic illustration of water wheel coverage. (c) Screening of optimal solutions for single-wheel configuration. (d) Screening of optimal solutions for double-wheel configuration. (e) Performance comparison and doubling rate analysis for the two prototype configurations at various flow rates. (f) Comparative analysis of output power between the two prototype configurations. (g) Assessment of the charging capacity of the WFEH-TENG. (h) Evaluation of the durability of the WFEH-TENG.

on water flow energy collection is thoroughly investigated to identify the optimal energy collection effect. The initial testing involves a single-wheel configuration, as shown in Fig. 4c, with a flow range varying from 120 L min^{-1} to 180 L min^{-1} and water wheel coverages ranging from 80% to 120%. The pulse frequency and I_{SC} of the device are tested. The results clearly show that the water wheel with 100% coverage outperforms others in terms of pulse frequency and I_{SC} across all flow rates. In addition, except for the water wheel with 100% coverage, the pulse frequency and I_{SC} of the other water wheels are 0 under specific flow rates due to their inability to overcome the magnetic field torques, resulting in non-rotation. For the double-wheel configuration, the first water wheel's coverage is set at 100% based on its optimal performance when subjected to the water flow. The second wheel's body parameters are then adjusted for testing. Fig. 4d reveals that the water wheel with 80% coverage exhibits the best output performance. Consequently, the decision is made to assemble two water wheels in tandem for the double-wheel configuration, with one having a coverage of 100% and the other having a coverage of 80%.

To validate the superiority of the double-wheel configuration in the actual water flow environment, its electrical outputs are compared with those of the single-wheel structure, as shown in Fig. 4e. With increasing flow rates from 120 L min^{-1} to 180 L min^{-1}, the pulse frequency of the single-wheel increases from 4.90 Hz to 38.51 Hz, whereas the pulse frequency I_{SC} of the double-wheel increases from 9.89 Hz to 67.60 Hz (Fig. 4e(i)). The I_{SC} ranges for the two configurations are 1.15 μA to 15.60 μA for the single-wheel and 2.87 μA to 34.20 μA for the double-wheel (Fig. 4e(ii)). In comparison, the pulse frequency of the double-wheel configuration is more than 1.75 times that of the single-wheel design, and the I_{SC} of the double-wheel configuration is more than 2.19 times that of the single-wheel design at any flow rate. A linear fitting analysis is conducted to explore the interrelation between frequency and flow rate. As depicted in Fig. S6, a distinct positive correlation is observed for both single and double wheels. This relationship can be primarily attributed to the influence of the water flow rate on the rotational speed of the water wheels, leading to changes in the relative slip velocity between friction materials and acceleration of charge transfer. Furthermore, the peak power of the two configurations is assessed under various resistance loads, as depicted in Fig. 4f. At a flow rate of 180 L min^{-1} and a load of 20 MΩ, the peak power of the single-wheel and double-wheel configurations reaches 2.65 mW and 10.76 mW, respectively, marking a 4.1-fold difference. For the peak and average power of the double-wheel configuration at the flow rate of 120 L min^{-1} to 170 L min^{-1}, please refer to Fig. S7. Fig. 4g illustrates that at a flow rate of 180 L min^{-1}, the WFEH-TENG effectively charges various commercial capacitors with different capacities, demonstrating its efficient charging capability. Additionally, at a flow rate of 180 L min^{-1}, the I_{SC} of WFEH-TENG can still maintain 95.8% of the initial I_{SC} after 300,000 times of continuous friction between the two friction materials, as shown in Fig. 4h. The experimental results presented above collectively underscore the remarkable water flow energy harvesting capabilities of the WFEH-TENG and emphasize the great value of ACT-TENG to the field of energy harvesting.

3.2. Demonstration of the ACT-TENG in the underground pipe gallery

The construction of underground smart pipeline galleries is of great importance in improving the intelligent management of cities. Various sensors are essential for the safe control and efficient operation of underground corridors. However, due to the complex air composition and unique spatial structure of the underground galleries, frequent manual maintenance is inconvenient and challenging. To ensure the smooth operation of sensor devices while simultaneously curbing maintenance expenses, incorporating a self-powered Internet of Things (IoT) system empowered by TENG technology emerges as a highly efficacious resolution. Fire protection, environmental monitoring, and intrusion alarm systems are essential for underground pipe galleries. Here, we harnessed WFEH-TENG to capture the kinetic energy from the fluid coursing through the pipelines, providing a sustainable power source for the essential components of these systems. The application scenario is vividly illustrated in Fig. 5a.

In Fig. 5b and Video S1, the WFEH-TENG continuously powers LED panels, serving as a critical resource for firefighting guidance. It ensures emergency visibility during critical situations. Additionally, Fig. 5c demonstrates the capability of the WFEH-TENG to drive wireless temperature and humidity sensors, which are essential for environmental monitoring. The WFEH-TENG efficiently charges a 1500 μF capacitor to 3.7 V in approximately 265 s. This stored energy is then used to power the temperature and humidity sensor, preventing accelerated equipment aging due to extreme temperature and humidity conditions, as illustrated in Fig. 5d and Video S2. Figs. 5e and 5f present the charge and discharge data, along with images showcasing the WFEH-TENG's role in constructing an intrusion alarm system for the underground smart pipe gallery. When an individual enters the monitoring range of the infrared induction module, the intrusion alarm system is activated, mitigating the risk of large-scale accidents or disruption within the corridor. The WFEH-TENG plays a vital role in this system by charging a 470 μF capacitor to 4.1 V within approximately 124 s. This charged capacitor enables the alarm system to detect target movements multiple times, as demonstrated in Video S3. These demonstrations collectively provide compelling evidence for the application potential of the WFEH-TENG in an underground smart pipe gallery. By efficiently converting the kinetic energy of fluid flow into usable electricity, the WFEH-TENG offers a sustainable and self-powered solution for powering vital systems, ensuring the smooth operation of smart pipe gallery, safety, and efficiency. It also again proves the superiority of the ACT-TENG output performance and the feasibility of its industrial application.

Supplementary material related to this article can be found online at doi:10.1016/j.nanoen.2023.109194.

Supplementary material related to this article can be found online at doi:10.1016/j.nanoen.2023.109194.

Supplementary material related to this article can be found online at doi:10.1016/j.nanoen.2023.109194.

4. Conclusion

In summary, we introduced a novel strategy, ACT-TENG (Accelerated Charge Transfer Triboelectric Nanogenerator), which achieved remarkable performance by accelerating the charge transfer while maintaining the material's original surface charge density. We demonstrated the feasibility of this strategy through the design and implementation of ACT-TENG, which combines an optimized magnetic field modulation mechanism with a bidirectional rotation mode, compared to conventional free-standing TENG (FS-TENG). Through rigorous testing, ACT-TENG achieved a peak power output of 5.27 mW at an input frequency of 1.0 Hz, representing a substantial 14.6-fold improvement over conventional FS-TENG. In practical terms, when charging a 100 μF capacitor to perform work under identical mechanical input conditions, FS-TENG and ACT-TENG delivered 0.09 mJ and 1.25 mJ of energy, respectively, showcasing a significant 13.9-fold difference. Moreover, ACT-TENG exhibited impressive electrical outputs, with an average current density of 2.14 mA m^{-2} Hz^{-1} and an average power density of 449.05 mW m^{-2} Hz^{-1}. These values represent substantial advancements compared to prior reports on FS-TENG. Furthermore, we designed and validated an integrated device for pipeline applications to highlight ACT-TENG's practical potential. By optimizing the water wheel's structure, we achieved a peak power output of 10.76 mW at a flow rate of 180 L min^{-1}. Finally, we constructed a self-powered IoT system for underground pipeline corridors based on ACT-TENG, encompassing functions such as fire protection, environmental monitoring, and intrusion alarm systems. Significantly, ACT-TENG's potential extends beyond water flow energy harvesting, encompassing a diverse array of applications in fields such as wind energy harvesting, high-voltage

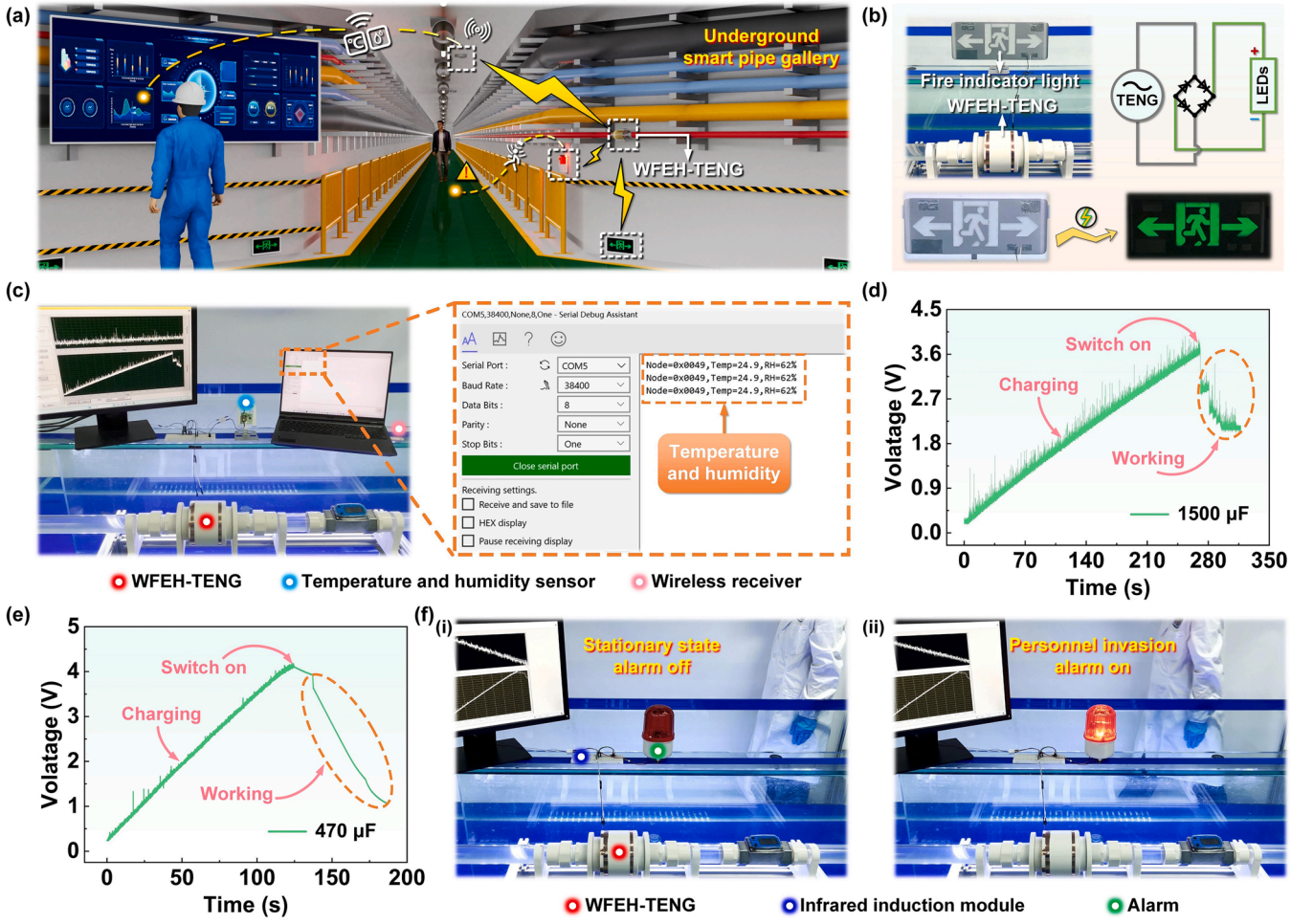

Fig. 5. The potential application of the WFEH-TENG in an underground smart pipe gallery. (a) Schematic representation of the potential WFEH-TENG application within an underground smart pipe gallery. (b) Demonstration of the WFEH-TENG powering LED panels for fire safety guidance. (c) Picture of the WFEH-TENG powering wireless temperature and humidity sensor operation. (d) The dynamic charging and discharging process of the WFEH-TENG for the wireless temperature and humidity sensor (e) The charging and discharging operation of the WFEH-TENG power supply for the infrared induction module. (f) Photographic representation of the intrusion alarm system.

power supply, and self-powered sensing. In conclusion, this study offers profound insights into the intricacies of TENG design and optimization and unveils a promising strategy with wide-reaching implications for industrial implementation.

5. Experimental section

Fabrication of the WFEH-TENG: The utilized water pipe boasts a diameter of 50 mm. The WFEH-TENG possesses specific dimensions: 282 mm in length, 122 mm in width, and 122 mm in height. The stator components of the WFEH-TEHG are interconnected through a 3D-printed shell and commercially available stainless steel fittings, employing a threaded fit. The water wheel is installed in the shell inside the casing through a standard commercial shaft and bearing components. The magnet features a thickness of 2 mm, while the ferromagnetic block measures 30 mm in length, 15 mm in width, and 0.5 mm in height. The copper foil used has a width of 22 mm. The internal configuration of the WFEH-TENG involves 16 copper foils securely adhered to the inner surface of a 3D-printed circular cylinder, boasting an inner diameter of 120 mm. These copper foils are uniformly distributed along the inner circumference. Additionally, the rotor is equipped with flexible blades, each with dimensions of 60 mm in length and 55 mm in width, designed to sweep the electrodes efficiently.

Measurement: The performance evaluation of the three operational modes was conducted using a precision rotating motor (Mode: J5718HBS401, China) to precisely control rotational speed. The electrical output generated by the WFEH-TENG was measured and analyzed using a high-precision electrometer (Keithley Mode 6514). Data acquisition and signal processing were accomplished with a dedicated computer-based system (National Instruments NI-USB-6356) in conjunction with LabVIEW 2018 software. The real-time monitoring of the dynamic torque and angular velocity of the rotor is accomplished with precision using a combined torque and velocity sensor (HDT15, China).

CRediT authorship contribution statement

Yushan Sun: Conceptualization, Investigation, Writing - Original Draft, Validation. **Yang Yu**: Investigation, Writing - Original Draft. **Qi Gao**: Investigation, Writing - Original Draft. **Xiaosong Zhang**: Investigation, Validation. **Jiacheng Zhang**: Investigation, Validation. **Yuqi Wang**: Validation, Editing. **Siyang He**: Validation, Editing. **Hengyu Li**: Conceptualization, Resources, Writing - review & editing, Supervision. **Zhong Lin Wang**: Conceptualization, Resources, Writing - review & editing, Supervision. **Tinghai Cheng**: Conceptualization, Resources, Writing - review & editing, Supervision.

Declaration of Competing Interest

The authors declare that they have no known competing financial interests or personal relationships that could have appeared to influence the work reported in this paper.

Data Availability

The data underpinning the findings of this study can be obtained from the corresponding author upon making a reasonable request.

Acknowledgments

Y. Sun, Y. Yu, and Q. Gao made equal contributions to this research. This research was supported by the National Key Research and Development Project granted by the Ministry of Science and Technology (Nos. 2021YFA1201601 & 2021YFA1201604).

Appendix A. Supporting information

Supplementary data associated with this article can be found in the online version at doi:10.1016/j.nanoen.2023.109194.

References

[1] Z.L. Wang, Entropy theory of distributed energy for internet of things, Nano Energy 58 (2019) 669–672.
[2] Q. Shi, B. Dong, T. He, Z. Sun, J. Zhu, Z. Zhang, C. Lee, Progress in wearable electronics/photonics—moving toward the era of artificial intelligence and internet of things, InfoMat 2 (6) (2020) 1131–1662.
[3] W. Liu, Z. Wang, C. Hu, Advanced designs for output improvement of triboelectric nanogenerator system, Mater. Today 45 (2021) 93–119.
[4] S. Chu, A. Majumdar, Opportunities and challenges for a sustainable energy future, Nat 488 (7411) (2012) 294–303.
[5] Y. Zhang, C.K. Jeong, J. Wang, X. Chen, K.H. Choi, L.-Q. Chen, W. Chen, Q. M. Zhang, Q. Wang, Hydrogel ionic diodes toward harvesting ultralow-frequency mechanical energy, Adv. Mater. 33 (36) (2021), 2103056.
[6] X. Zhao, A. Nashalian, I.W. Ock, S. Popoli, J. Xu, J. Yin, T. Tat, A. Libanori, G. Chen, Y. Zhou, J. Chen, A soft magnetoelastic generator for wind-energy harvesting, Adv. Mater. 34 (38) (2022), 2204238.
[7] F.-R. Fan, Z.-Q. Tian, Z.L. Wang, Flexible triboelectric generator, Nano Energy 1 (2) (2012) 328–334.
[8] C. Zhang, W. Tang, C. Han, F. Fan, Z.L. Wang, Theoretical comparison, equivalent transformation, and conjunction operations of electromagnetic induction generator and triboelectric nanogenerator for harvesting mechanical energy, Adv. Mater. 26 (22) (2014) 3580–3591.
[9] Z.L. Wang, On Maxwell's, displacement current for energy and sensors: the origin of nanogenerators, Mater. Today 20 (2) (2017) 74–82.
[10] Z.L. Wang, A.C. Wang, On the origin of contact-electrification, Mater. Today 30 (2019) 34–51.
[11] H. Zou, Y. Zhang, L. Guo, P. Wang, X. He, G. Dai, H. Zheng, C. Chen, A.C. Wang, C. Xu, Z.L. Wang, Quantifying the triboelectric series, Nat. Commun. 10 (1) (2019), 1427.
[12] Z.L. Wang, On the first principle theory of nanogenerators from Maxwell's equations, Nano Energy 68 (2020), 104272.
[13] Y. Wang, X. Yu, M. Yin, J. Wang, Q. Gao, Y. Yu, T. Cheng, Z.L. Wang, Gravity triboelectric nanogenerator for the steady harvesting of natural wind energy, Nano Energy 82 (2021), 105740.
[14] Z. Ren, L. Wu, Y. Pang, W. Zhang, R. Yang, Strategies for effectively harvesting wind energy based on triboelectric nanogenerators, Nano Energy 100 (2022), 107522.
[15] S. Zhang, Z. Jing, X. Wang, K. Fan, H. Zhao, Z.L. Wang, T. Cheng, Enhancing low-velocity water flow energy harvesting of triboelectric–electromagnetic generator via biomimetic-fin strategy and swing-rotation mechanism, ACS Energy Lett. 7 (12) (2022) 4282–4289.
[16] Z. Deng, L. Xu, H. Qin, X. Li, J. Duan, B. Hou, Z.L. Wang, Rationally structured triboelectric nanogenerator arrays for harvesting water-current energy and self-powered sensing, Adv. Mater. 34 (39) (2022), 2205064.
[17] H. Luo, J. Liu, T. Yang, Y. Zhang, Q. Cao, Dipteran flight-inspired bistable triboelectric nanogenerator for harvesting low frequency vibration, Nano Energy 103 (2022), 107755.
[18] Y. Qi, Y. Kuang, Y. Liu, G. Liu, J. Zeng, J. Zhao, L. Wang, M. Zhu, C. Zhang, Kirigami-inspired triboelectric nanogenerator as ultra-wide-band vibrational energy harvester and self-powered acceleration sensor, Appl. Energy 327 (2022), 120092.
[19] Q. Gao, Y. Xu, X. Yu, Z. Jing, T. Cheng, Z.L. Wang, Gyroscope-structured triboelectric nanogenerator for harvesting multidirectional ocean wave energy, ACS Nano 16 (4) (2022) 6781–6788.
[20] X. Liang, S. Liu, S. Lin, H. Yang, T. Jiang, Z.L. Wang, Liquid–solid triboelectric nanogenerator arrays based on dynamic electric-double-layer for harvesting water wave energy, Adv. Energy Mater. 13 (24) (2023), 2300571.
[21] B. Chen, Y. Yang, Z.L. Wang, Scavenging wind energy by triboelectric nanogenerators, Adv. Energy Mater. 8 (10) (2018), 1702649.
[22] M. Zhu, Z. Sun, T. Chen, C. Lee, Low cost exoskeleton manipulator using bidirectional triboelectric sensors enhanced multiple degree of freedom sensory system, Nat. Commun. 12 (1) (2021), 2692.
[23] G. Khandelwal, N.P. Maria Joseph Raj, S.-J. Kim, Materials beyond conventional triboelectric series for fabrication and applications of triboelectric nanogenerators, Adv. Energy Mater. 11 (33) (2021), 2101170.
[24] Y. Yu, H. Li, D. Zhao, Q. Gao, X. Li, J. Wang, Z.L. Wang, T. Cheng, Material's selection rules for high performance triboelectric nanogenerators, Mater. Today 64 (2023) 61–71.
[25] B. Dudem, D.H. Kim, A.R. Mule, J.S. Yu, Enhanced performance of microarchitectured PTFE-based triboelectric nanogenerator via simple thermal imprinting lithography for self-powered electronics, ACS Appl. Mater. Interfaces 10 (28) (2018) 24181–24192.
[26] S. Niu, Y. Liu, S. Wang, L. Lin, Y.S. Zhou, Y. Hu, Z.L. Wang, Theory of sliding-mode triboelectric nanogenerators, Adv. Mater. 25 (43) (2013) 6184–6193.
[27] S. Niu, Y. Liu, S. Wang, L. Lin, Y.S. Zhou, Y. Hu, Z.L. Wang, Theoretical investigation and structural optimization of single-electrode triboelectric nanogenerators, Adv. Funct. Mater. 24 (22) (2014) 3332–3340.
[28] S. Wang, Y. Xie, S. Niu, L. Lin, Z.L. Wang, Freestanding triboelectric-layer-based nanogenerators for harvesting energy from a moving object or human motion in contact and non-contact modes, Adv. Mater. 26 (18) (2014) 2818–2824.
[29] S. Fu, W. He, Q. Tang, Z. Wang, W. Liu, Q. Li, C. Shan, L. Long, C. Hu, H. Liu, An ultrarobust and high-performance rotational hydrodynamic triboelectric nanogenerator enabled by automatic mode switching and charge excitation, Adv. Mater. 34 (2) (2022), 2105882.
[30] Z. Liu, Y. Huang, Y. Shi, X. Tao, H. He, F. Chen, Z.-X. Huang, Z.L. Wang, X. Chen, J.-P. Qu, Fabrication of triboelectric polymer films via repeated rheological forging for ultrahigh surface charge density, Nat. Commun. 13 (1) (2022), 4083.
[31] Y. Yu, Q. Gao, X. Zhang, D. Zhao, X. Xia, J. Wang, H. Li, Z.L. Wang, T. Cheng, Contact-sliding-separation mode triboelectric nanogenerator, Energy Environ. Sci. 16 (9) (2023) 3932–3941.
[32] X. Li, C. Zhang, Y. Gao, Z. Zhao, Y. Hu, O. Yang, L. Liu, L. Zhou, J. Wang, Z. L. Wang, A highly efficient constant-voltage triboelectric nanogenerator, Energy Environ. Sci. 15 (3) (2022) 1334–1345.
[33] H. Wu, W. He, C. Shan, Z. Wang, S. Fu, Q. Tang, H. Guo, Y. Du, W. Liu, C. Hu, Achieving remarkable charge density via self-polarization of polar high-k material in a charge-excitation triboelectric nanogenerator, Adv. Mater. 34 (13) (2022), 2109918.
[34] W. He, C. Shan, S. Fu, H. Wu, J. Wang, Q. Mu, G. Li, C. Hu, Large harvested energy by self-excited liquid suspension triboelectric nanogenerator with optimized charge transportation behavior, Adv. Mater. 35 (7) (2023), 2209657.
[35] G. Du, J. Wang, Y. Liu, J. Yuan, T. Liu, C. Cai, B. Luo, S. Zhu, Z. Wei, S. Wang, S. Nie, Fabrication of advanced cellulosic triboelectric materials via dielectric modulation, Adv. Sci. 10 (15) (2023), 2206243.
[36] M. Shanbedi, H. Ardebili, A. Karim, Polymer-based triboelectric nanogenerators: materials, characterization, and applications, Prog. Polym. Sci. 144 (2023), 101723.
[37] Y. Bai, L. Xu, S. Lin, J. Luo, H. Qin, K. Han, Z.L. Wang, Charge pumping strategy for rotation and sliding type triboelectric nanogenerators, Adv. Energy Mater. 10 (21) (2020), 2000605.
[38] J. Wang, X. Yu, D. Zhao, Y. Yu, Q. Gao, T. Cheng, Z.L. Wang, Enhancing output performance of triboelectric nanogenerator via charge clamping, Adv. Energy Mater. 11 (31) (2021), 2101356.

Yushan Sun was born in Jilin Province, China in 1998, he graduated from Changchun University of Technology, China in 2020 with a B.E. degree in mechanical engineering. He is currently studying for an M.S. in mechanical engineering at Changchun University of Technology. And he is currently a visiting student at Beijing Institute of Nanoenergy and Nanosystems. His research interests include triboelectric nanogenerators and self-powered sensors.

Yang Yu was born in 1995 Jilin province, majored in mechanical engineering, and achieved the B.E. and M.S. degrees from Changchun University of Technology. He is currently pursuing Ph.D. degree in Beijing Institute of Nanoenergy and Nanosystems, Chinese Academy of Sciences. His research interest is triboelectric nanogenerator.

Qi Gao was born in 1995 Jilin province, majored in mechanical engineering, and achieved the B.S. and M.S. degree from Changchun University of Technology in 2017 and 2020, respectively. He continues pursuing Ph.D. degree in Beijing Institute of Nanoenergy and Nanosystems. His research interest is triboelectric nanogenerator.

Xiaosong Zhang was born in Sichuan province, China, in 1996. He received his B.E. and M.E. degrees in mechanical engineering from Changchun University of Technology, China, in 2019 and 2022, respectively, and he is currently pursuing a Ph.D. degree in Beijing Institute of Nanoenergy and Nanosystems, Chinese Academy of Sciences. His research interests mainly focus on vibration triboelectric nanogenerator and triboelectric mechanical sensors.

Jiacheng Zhang received his B.S. in School of Mechanical Engineering from Harbin University of Science and Technology, China, in 2018. He received his M.S. degree in School of Mechanical Engineering from Wuhan University of Science and Technology in 2021. He is currently a Ph.D. candidate in the same school. His research interests include fluid dynamics and fluid–structure interaction.

Yuqi Wang was born in 1995 Jilin province, majored in mechatronic engineering and achieved the B.E. degree from the Changchun University of Technology in 2018. He continues pursuing a Master of Engineering degree in the same school. He is currently pursuing Ph.D. degree at Beijing Institute of Nanoenergy and Nanosystems. His research interests are environmental energy harvesting through triboelectric nanogenerators.

Siyang He was born in 1997 Heilongjiang province, majored in mechanical engineering, and achieved the B.S. and M.S. degree from Changchun University of Technology in 2019 and 2023, respectively. He is currently pursuing Ph.D. degree in Beijing Institute of Nanoenergy and Nanosystems, Chinese Academy of Sciences. His research interest is triboelectric nanogenerator.

Hengyu Li was born in Jilin province, China, in 1991. He received his B.E. and M.E. degrees in mechanical engineering from the School of Mechatronics Engineering at Changchun University of Technology, China, in 2015 and 2018, respectively. He received his Ph.D. degree in mechanical engineering from the School of Mechatronics Engineering at Harbin Institute of Technology, China, in 2022. He is currently a postdoctoral fellow at Beijing Institute of Nanoenergy and Nanosystems, Chinese Academy of Sciences, China. His research interests include triboelectric nanogenerator (TENG), environmental energy harvester, piezoelectric micro jets, and piezoelectric micro pumps, piezoelectric actuators.

Prof. Zhong Lin Wang received his Ph.D. from Arizona State University in physics. He now is the Hightower Chair, Regents' Professor, Engineering Distinguished Professor and Director, Center for Nanostructure Characterization, at Georgia Tech. Dr. Wang has made original and innovative contributions to the synthesis, discovery, characterization and understanding of fundamental physical properties of oxide nanobelts and nanowires, as well as applications of nanowires in energy sciences, electronics, optoelectronics and biological science. His discovery and breakthroughs in developing nanogenerators established the principle and technological road map for harvesting mechanical energy from environment and biological systems for powering personal electronics. His research on self-powered nanosystems has inspired the worldwide effort in academia and industry for studying energy for micro-nano-systems, which is now a distinct disciplinary in energy research and future sensor networks. He coined and pioneered the field of piezotronics and piezophototronics by introducing piezoelectric potential gated charge transport process in fabricating new electronic and optoelectronic devices. Details can be found at: http://www.nanoscience.gatech.edu.

Prof. Tinghai Cheng received the B.S., M.S. and Ph.D. degrees from Harbin Institute of Technology in 2006, 2008 and 2013, respectively. He was a visiting scholar in the School of Materials Science and Engineering at Georgia Institute of Technology from 2017 to 2018. Currently, he is a professor of Beijing Institute of Nanoenergy and Nanosystems, Chinese Academy of Sciences. His research interests are triboelectric nanogenerators, piezoelectric energy harvester, and piezoelectric actuators.